

Achromatic on-chip focusing of graphene plasmons for spatial inversions of broadband digital optical signals

Zhiyong Wu^{a,b} and Zhengji Xu^{a,b,*}

^aSun Yat-sen University, School of Microelectronics Science and Technology, Zhuhai, China

^bSun Yat-sen University, Guangdong Provincial Key Laboratory of Optoelectronic Information Processing Chips and Systems, Zhuhai, China

Abstract. On-chip focusing of plasmons in graded-index lenses is important for imaging, lithography, signal processing, and optical interconnects at the deep subwavelength nanoscale. However, owing to the inherent strong wavelength dispersion of plasmonic materials, the on-chip focusing of plasmons suffers from severe chromatic aberrations. With the well-established planar dielectric grating, a graded-index waveguide array lens (GIWAL) is proposed to support the excitation and propagation of acoustic graphene plasmon polaritons (AGPPs) and to achieve the achromatic on-chip focusing of the AGPPs with a focus as small as about 2% of the operating wavelength in the frequency band from 10 to 20 THz, benefiting from the wavelength-independent index profile of the GIWAL. An analytical theory is provided to understand the on-chip focusing of the AGPPs and other beam evolution behaviors, such as self-focusing, self-collimation, and pendulum effects of Gaussian beams as well as spatial inversions of digital optical signals. Furthermore, the possibility of the GIWAL to invert spatially broadband digital optical signals is demonstrated, indicating the potential value of the GIWAL in broadband digital communication and signal processing.

Keywords: achromatic lens; self-focusing lens; graded-index lens; waveguide array; broadband focusing; graphene plasmon.

Received Apr. 14, 2023; revised manuscript received Jun. 23, 2023; accepted for publication Jul. 5, 2023; published online Jul. 24, 2023.

© The Authors. Published by SPIE and CLP under a Creative Commons Attribution 4.0 International License. Distribution or reproduction of this work in whole or in part requires full attribution of the original publication, including its DOI.

[DOI: [10.1117/1.APN.2.5.056003](https://doi.org/10.1117/1.APN.2.5.056003)]

1 Introduction

On-chip integrated photonic devices exhibit great potential for applications in many fields, including optical communications,^{1,2} quantum gates,^{3,4} signal processing,^{5,6} and computing.^{7,8} To fully demonstrate the functionalities of integrated photonic devices, it is essential to manipulate on-chip photonic modes like controlling free-space light beams, such as beam focusing, bending, and steering.^{9,10} As primary functions, these manipulations are basic elements for the creation of further devices and systems. For example, the graded-index waveguide-based on-chip focusing lenses have been used as mode spot size converters and $4f$ systems,^{11–14} Eaton lenses have been utilized as on-chip waveguide bends,^{15,16} and Maxwell's fish-eye lenses have been demonstrated as multimode waveguide crossings.^{17,18} However, owing to the sensitive wavelength dependence of the

waveguide mode, these lenses are usually only suitable for specific operating wavelengths. Moreover, due to the diffraction limit of light, lateral dimensions of these structures are often relatively large, resulting in a much lower level of integration and miniaturization than that achievable in modern electronics.

The continued pursuit in highly integrated nanophotonic circuits has fueled the flourishing of surface plasmon polaritons (SPPs) (electromagnetic waves coupled to collective oscillations of free electrons in a conductor)^{19–21} because they can circumvent the diffraction limit and confine light to deep subwavelength scales, enabling nanoscale optoelectronic components. With the rapid development of material science and nanofabrication, many photonic functionalities based on the on-chip focusing of the SPPs supported by the graded-index waveguide structures have been realized, such as the sorting of the orbital angular momentum of light,^{22,23} the manipulation of the longitudinal trajectory of the beam,^{24,25} and the spatiotemporal operation of optical pulses.^{26,27} Nonetheless, the on-chip focusing

*Address all correspondence to Zhengji Xu, xuzhj27@mail.sysu.edu.cn

of the SPPs still faces a formidable challenge of the severe chromatic aberration due to the inherent strong wavelength dispersion of plasmonic materials, which limits its further applications in the multicolor manipulation and broadband operation. Furthermore, to process ultrashort on-chip optical pulse signals at the nanoscale, it is very urgent to achieve the achromatic on-chip focusing of the SPPs,²⁸ which also enables expanding the capacity of nanoscale on-chip photonic devices.

Because of its two-dimensional nature and thus all surfaces, as well as its negative effective permittivity, graphene has been shown to support SPPs called graphene plasmon polaritons (GPPs)—electromagnetic waves coupled to collective oscillations of conduction band electrons within graphene—in the mid-infrared (MIR) to terahertz (THz) spectrum,^{29–31} considered an important frequency band for the molecular fingerprint detection and next-generation communication technology.^{32–34} The excellent properties of the extreme confinement and low loss of the GPPs enable many miniaturized on-chip optoelectronic devices in the long-wavelength spectrum.^{35,36} Unfortunately, the on-chip focusing of the GPPs supported by single-layer graphene still exhibits large chromatic aberrations³⁷ due to the quadratic dispersion relationship of the GPPs.³⁰ Very recently, a class of highly confined antisymmetric GPP modes called acoustic GPPs (AGPPs) has been demonstrated by placing graphene near a metallic surface.^{38–40} The AGPPs show a linear dispersion relationship between the energy and momentum,^{30,39} suggesting the possibility of the achromatic on-chip focusing of these polaritons. Furthermore, recent experimental observations prove that the AGPPs with a mode size of only a few nanometers can be excited by both near-field and far-field methods, unquestionably confirming the practicality of the on-chip generation and manipulation of the AGPPs.^{38,41,42}

In this work, based on the well-established planar dielectric grating and the concept of graded-index materials, we propose a practical stratagem to achieve the achromatic on-chip focusing of the AGPPs by devising a graded-index waveguide array lens (GIWAL). By studying the mode properties of the AGPPs supported by the GIWAL, we provide an analytical model to understand the complete physics underlying the on-chip focusing and other beam evolution behaviors, such as self-focusing, self-collimation, and pendulum effects of Gaussian beams as well as spatial inversions of digital optical signals, which are attributed to the superposition of all orthogonal AGPP modes along the propagation direction. The designed GIWAL, which resembles the Mikaelian lens developed from well-known Maxwell's fish-eye lens by utilizing conformal transformation optics,^{43,44} can converge periodically light waves at the central axis of the lens. By adjusting the filling factor of the dielectric grating in the GIWAL, the modal index of the lens is designed and thus the desired graded index profile of Mikaelian lens is obtained, which can be analytically understood and quantitatively predicted with the effective index method of the AGPPs propagating in a periodic two-medium slab waveguide. The theoretical designs certified by numerical simulations prove how the achromatic on-chip focusing of the AGPPs with a focus as small as about 0.02λ (λ is the working wavelength in free space) within the frequency band from 10 to 20 THz can be achieved in the GIWAL. As an application case, we establish the possibility of using the GIWAL as a spatial inverter for broadband digital optical signals. The high agreement between theoretical results and numerical simulations from COMSOL Multiphysics confirms the immense potential of the presented analytical scheme for

greatly simplifying the design of such a configuration in experimental fabrication.

2 Results and Discussion

Figure 1(a) schematically reveals the proposed scenario to support the excitation and propagation of the AGPPs and to achieve the achromatic on-chip focusing of the AGPPs based on the GIWAL, which could be fabricated by covering graphene onto a dielectric grating on top of a metallic substrate. In such a structure, as one of the possible methods, with the diffraction from the coupling grating, the z -polarized light incident along the y direction could be coupled to the AGPPs maintained at the dielectric grating between the metallic substrate and graphene and traveling along the z axis (see Sec. 3 in the [Supplementary Material](#) for coupling details). The cross section of the GIWAL is shown in Fig. 1(b). In the frequency band we consider, the metallic substrate acts like a perfect electrical conductor, which can insulate the diffusion of the electromagnetic field, thereby reducing the size of the AGPP modes and further increasing the concentration of the electromagnetic energy. The whole configuration is surrounded by air, and thus $\epsilon_1 = \epsilon_{22} = 1$. Furthermore, the dielectric grating is envisioned as SiO_2 of thickness $d = 20$ nm and relative permittivity $\epsilon_{21} = 2.25$. The grating period Λ is fixed at 150 nm, whereas the dielectric strip's width a in each unit cell is variable, which allows one to obtain a desired mode index profile by rationally arranging dielectric strips of suitable widths.

According to the idea of the effective index method,^{45–47} for the propagating of the AGPPs along the z direction, each unit cell constituting the GIWAL can be regarded as a homogeneous medium characterized by an effective refractive index n_{eff} . Moreover, the inherent loss of the AGPP mode caused by the metallic substrate and graphene is implied by its propagation length L . Based on the proposed analytical model (see Sec. 1 in the [Supplementary Material](#) for details), the dependences of the effective refractive index and the propagation length of the AGPPs on the width of the dielectric strip are calculated, as shown in Figs. 1(c) and 1(d), respectively. The fact that n_{eff} is much larger than the refractive index of the SiO_2 grating indicates that the AGPPs have high mode confinement, as shown in Fig. S1(d) in the [Supplementary Material](#). Figure 1(d) indicates that the AGPP modes can propagate tens of micrometers' distance, which is much larger than the AGPP wavelength in the GIWAL. As a increases, the dielectric strip of a greater refractive index occupies more space in the grating, resulting in a larger n_{eff} , corresponding to a stronger mode field confinement usually. A stronger field confinement is accompanied by a larger mode loss and thus a smaller propagation length of the AGPPs. Furthermore, reducing the wavelength of the incident light brings a greater mode field concentration and thus a larger n_{eff} and a smaller L , as shown in Figs. 1(c) and 1(d). The circles, triangles, and squares on the corresponding curves in Figs. 1(c) and 1(d) are the results from numerical simulations performed by COMSOL Multiphysics. The great agreement between theoretical results and numerical simulations confirms the validity of the proposed analytical approach. Most importantly, the trend of n_{eff} versus a is wavelength-independent, as shown by the normalized n_{eff} in Fig. 1(c). As discussed later, this performance is a precondition for achieving achromatic on-chip focusing of the AGPPs in the GIWAL. In addition, the effect of other parameters, such as the relaxation rate and the chemical potential of graphene and the thickness, period, and relative permittivity of

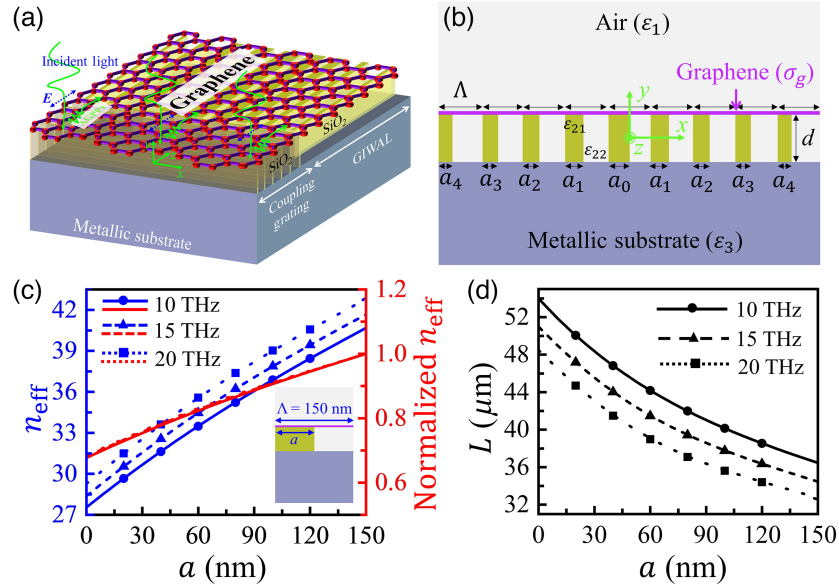


Fig. 1 Achromatic on-chip focusing lenses and mode properties of the AGPPs propagating within a single unit cell of the GIWAL. (a) Schematic structure of the coupling grating and the GIWAL. (b) Cross section of the GIWAL and Cartesian coordinate system employed. Dependences of (c) the effective refractive index and (d) the propagation length of the AGPPs on the width of the dielectric strip for different frequencies of the incident lights. The solid and dashed curves represent analytic results, and the circles, triangles, and squares on the corresponding curves represent numerical simulations. The inset in (c) represents the cross section of a single unit cell of the GIWAL.

the dielectric grating, on this performance is also discussed in Sec. 2 in the [Supplementary Material](#). Moreover, our proposed theoretical model can directly include the analysis for the hybridization between the AGPPs and phonons of the SiO₂ grating.³⁰ As discussed in Sec. 4 in the [Supplementary Material](#), the AGPP–phonon hybridization significantly reshapes the dispersion curve of the original pure AGPPs and leads to the emergence of new mixing modes. As a proof-of-concept demonstration, this hybridization effect will not be considered in the following analysis. In practical experiments, to avoid the plasmon–phonon hybridization, dielectric gratings with phonon resonances outside the operating frequency band should be selected.

To achieve the achromatic on-chip focusing of the AGPPs, the effective refractive index distribution of the GIWAL needs to satisfy a certain function. To find the form of the function, we briefly turn our attention back to the well-known Mikaelian lens. The refractive index profile of Mikaelian lens, which can be extracted from Maxwell’s fish-eye lens by an exponential conformal mapping, exhibits a symmetrical distribution of $n(x) = n_0 \operatorname{sech}(\xi x)$,^{43,44,48} as shown by the red curve in Fig. 2(a), where ξ is the gradient coefficient and n_0 is the maximum refractive index at the central axis of the lens. Within the framework of geometric optics, light is regarded as classical particles, and the only thing that matters is its trajectories. According to the eikonal theory and the variational method, the trajectory equation of the light ray incident perpendicular to the x axis on the $y = 0$ plane in the Mikaelian lens can be derived as (see Sec. 5 in the [Supplementary Material](#) for details)

$$x(z) = \frac{1}{\xi} \sinh^{-1} \left[\sin \left(\xi z + \frac{\pi}{2} \right) \sinh(\xi x_0) \right], \quad (1)$$

where x_0 is the incident point of the ray on the x axis. It can be found from Eq. (1) that the rays converge periodically at $z = (2v - 1)\pi/(2\xi)$ ($v = 1, 2, 3, \dots$) on the central axis of the lens by setting $x = 0$. Thus we can extract the focal length of the Mikaelian lens as $f_L = \pi/(2\xi)$. Importantly, the focal length f_L does not depend on the specific value of the refractive index (i.e., n_0), but only on the changing trend of the refractive index, i.e., ξ . Based on Eq. (1), the trajectories of rays as shown by red curves in Fig. 2(d) indicate that the Mikaelian lens is naturally free of spherical aberration, since off-axis and paraxial rays converge to the same focal point. This property makes the lens useful in high-quality imaging systems and optoelectronic components independent of mode field distributions, such as mode-independent spot-size converters, because the electromagnetic energy of the off-axis portion of higher-order modes can be brought to the same focal point on the central axis.

As a demonstration case, the GIWAL is assumed to have 61 unit cells, as shown in Fig. S7 in the [Supplementary Material](#). To satisfy the refractive index profile of the Mikaelian lens with a focal length of $f_L = 10 \mu\text{m}$ shown by the red curve in Fig. 2(a), the widths of the dielectric strip of each unit cell in the GIWAL (a_0, a_1, \dots, a_{30}) are set as 130.0, 129.9, 129.4, 128.7, 127.7, 126.4, 124.8, 123.0, 120.9, 118.6, 116.0, 113.2, 110.2, 107.0, 103.5, 99.9, 96.2, 92.3, 88.2, 84.1, 79.8, 75.5, 71.0, 66.5, 62.0, 57.4, 52.8, 48.2, 43.6, 39.0, and 34.4 nm, respectively, according to the theoretically calculated dependence of n_{eff} on a shown in Fig. 1(c). The refractive index profile of this precise GIWAL is shown as the green curve in Fig. 2(a). To improve the tolerance for manufacturing errors, the step in the dielectric strip’s width is chosen to be 5 nm, thus (a_0, a_1, \dots, a_{30}) become 130, 130, 130, 130, 125, 125, 125, 120, 120, 115, 115, 110, 105,

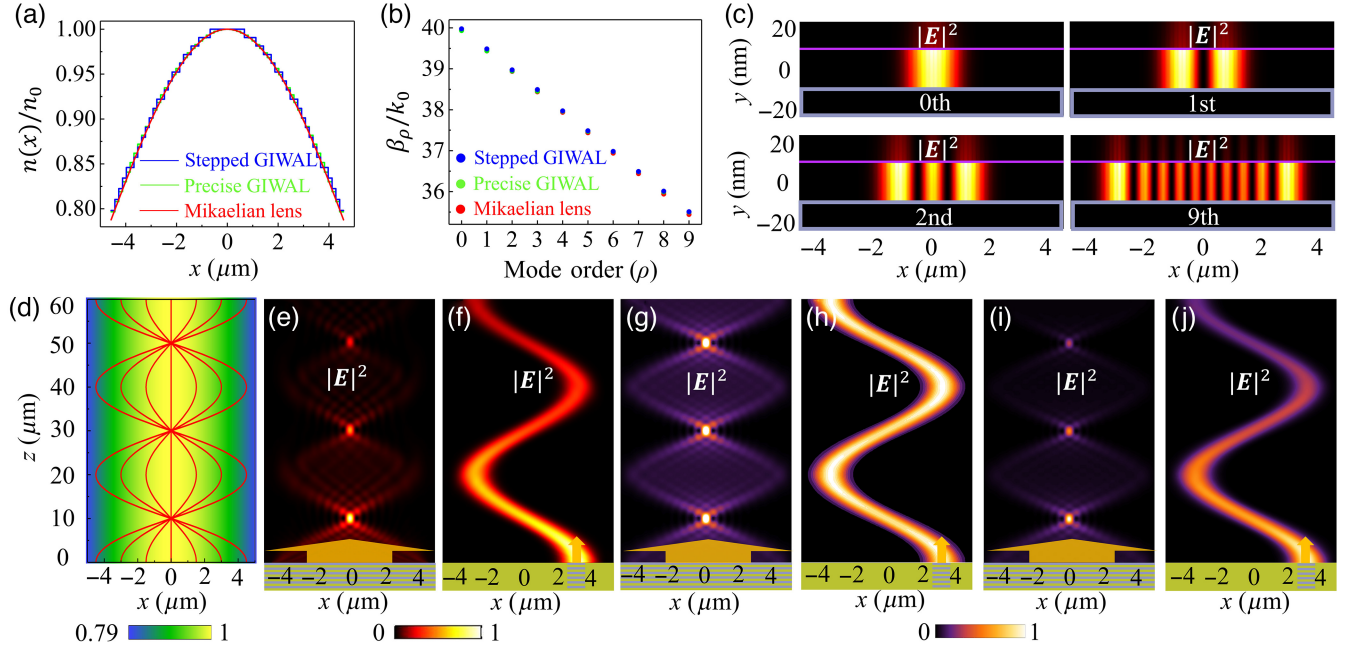


Fig. 2 On-chip focusing and optical pendulum effects of the AGPPs in the GIWAL and mode properties of the AGPPs supported by the entire GIWAL. (a) Refractive index profile and (b) the propagation constant of the waveguide modes for Mikaelian lens (red), precise GIWAL (green), and stepped GIWAL (blue), respectively. (c) Normalized electric field $|E|^2$ of the 0th, 1st, 2nd, and 9th order AGPP modes on the cross section of the stepped GIWAL. The purple line, the gray box, and the area between them indicate the locations of graphene, metallic substrate, and SiO_2 grating, respectively. (d) Both the trajectories of rays and the refractive index profile on the $y = 0$ plane in Mikaelian lens. Evolutions of the normalized electric field $|E|^2$ of the AGPPs on the $y = 0$ plane in the stepped GIWAL for (e), (f) numerical simulations with losses and analytical results (g), (h) without losses and (i), (j) with losses, respectively. The broad arrows in (e), (g), and (i) represent the incident lights coupled to the AGPPs through the extended coupling grating, whereas the narrow arrows in (f), (h), and (j) represent the incident lights coupled to the AGPPs through the local coupling grating. The frequency of the incident light is $f = 15$ THz, and the focal length of the on-chip focusing is $f_L = 10 \mu\text{m}$.

105, 100, 95, 90, 90, 85, 80, 75, 70, 65, 60, 55, 55, 50, 45, 40, and 35 nm, respectively. The refractive index profile of this stepped GIWAL is shown as the blue curve in Fig. 2(a). There is no essential difference in the propagation properties of the AGPPs between the two GIWALs, as shown in Fig. S8 in the [Supplementary Material](#). We first apply an extended coupling grating to couple the incident light to the AGPP modes, which then propagate along the z direction in the GIWAL. The normalized electric field $|E|^2$ of the AGPPs on the $y = 0$ plane in the stepped GIWAL is shown in Fig. 2(e). The AGPPs achieve periodic focusing at $z = (2v - 1)\pi/(2\xi)$ in the stepped GIWAL, confirming the validity of the theoretical design. Furthermore, owing to the inherent loss of the AGPPs, the focusing energy gradually decreases with increasing propagation distance. The counterpart of Fig. 2(e) excluding losses is shown in Fig. S9(a) in the [Supplementary Material](#). By comparing Fig. 2(e) and Fig. S9(a) in the [Supplementary Material](#), it can be found that losses do not affect the overall behavior of the on-chip focusing, except for weakening the magnitude of the electric field of the AGPP modes. Figure 2(f) reveals the normalized electric field $|E|^2$ of the AGPPs coupled by the local coupling grating, exhibiting an analog of the optical pendulum effect. The energy flow is very consistent with the ray trajectory

from geometrical optics shown in Fig. 2(d). For comparison, the corresponding $|E|^2$ without losses is shown in Fig. S9(b) in the [Supplementary Material](#). The wonderful identity between ray trajectories within geometrical optics and numerical simulations based on wave optics could be attributed to two reasons. On the one hand, each unit cell can be viewed as a homogeneous medium characterized by the corresponding effective refractive index because the AGPP wavelength is much larger than the period Λ of the GIWAL. On the other hand, since the AGPP wavelength is much smaller than the GIWAL scale, the light-ray approximation is satisfied.⁴³ This excellent property suggests that our proposed GIWAL could work in the geometrical optics limit and wave optics fields simultaneously.

To further understand the physical process of the on-chip focusing and the beam evolution, we now analyze propagation properties of the AGPPs supported by the entire GIWAL based on wave optics. For simplicity, we ignore losses here, which do not destroy the physical nature of the on-chip focusing and the beam evolution, as mentioned above. Continuing the effective index method used above, the entire GIWAL resembles a waveguide with a graded refractive index of $n(x) = n_0 \text{sech}(\xi x)$. Since the electric field of the AGPPs lies mainly on the y axis, they are transverse electric modes propagating along the

z direction for this effective waveguide. Thus the dispersion relation satisfied by the AGPPs can be written as (see Sec. 9 in the [Supplementary Material](#) for details)

$$\beta_\rho = \sqrt{k_0^2 n_0^2 + \frac{1}{4} \xi^2} - \left(\rho + \frac{1}{2} \right) \xi, \quad (2)$$

where k_0 is the wavenumber of the incident light in vacuum, $\rho = 0, 1, 2, \dots$ is the mode order, and β_ρ is the propagation constant of the ρ th order AGPP mode along the z axis. The propagation constants of the first 10 AGPP modes are shown in Fig. 2(b), including the analytical results from Eq. (2) and numerical results of the precise and stepped GIWALs. The good agreement among these results confirms the validity of the analytical theory. As the mode order increases, the electric field of the AGPPs expands from the center to the edge of the GIWAL, where the refractive index is smaller, resulting in a decrease in the propagation constant. Moreover, the normalized electric

field $|E|^2$ of the zeroth, first, second, and ninth order AGPP modes on the cross section of the stepped GIWAL are shown in Fig. 2(c). The distributions of $|E|^2$ show that the energy of the AGPPs is almost completely confined into the dielectric grating between the graphene and the metallic substrate, revealing the practicality of the on-chip focusing with mode sizes of only tens of nanometers along the y axis. Furthermore, the distributions of $|E|^2$ of the AGPP modes on the line of $y = 0$ in the stepped GIWAL are also consistent with the theoretical results, as shown in Fig. S11 in the [Supplementary Material](#).

According to the analytical theory described in Sec. 9 in the [Supplementary Material](#), the electric field component of the ρ th order AGPP mode along the y axis on the $y = 0$ plane in the GIWAL is

$$E_{y\rho}(x, z) = A_\rho Q_\rho(x) e^{i\beta_\rho z}, \quad (3)$$

where

$$Q_\rho(x) = \begin{cases} {}_2F_1[S_1, S_2, S_3, -\sinh^2(\xi x)] \operatorname{sech}^s(\xi x) & \text{for } \rho = 0, 2, 4, \dots \\ {}_2F_1[S_1 - S_3 + 1, S_2 - S_3 + 1, 2 - S_3, -\sinh^2(\xi x)] \sinh(\xi x) \operatorname{sech}^s(\xi x) & \text{for } \rho = 1, 3, 5, \dots \end{cases} \quad (4)$$

in which ${}_2F_1$ is a Gaussian hypergeometric function, $S_1 = (\rho - 2s)/2$, $S_2 = -\rho/2$, $S_3 = 1/2$, and $s = [(1 + 4k_0^2 n_0^2 / \xi^2)^{1/2} - 1]/2$, respectively. Moreover, the normalization constant for the ρ th order AGPP mode is calculated using

$$A_\rho = \left(\frac{1}{\int_{-\infty}^{\infty} |Q_\rho(x)|^2 dx} \right)^{1/2}. \quad (5)$$

The coupling grating can couple the incident light to the AGPP modes, which then propagate along the z direction to the incident end of the GIWAL. The polaritons at the incident end can excite different orders of the AGPP modes supported by the GIWAL, and these modes then interfere with each other, generating different intensity patterns in the GIWAL depending on the profile of the light beam at the incident end. If the electric field at the incident end of the GIWAL is $E_y(x, 0)$ at $z = 0$, its evolution on the $y = 0$ plane in the GIWAL can be represented by the superposition of all orthogonal AGPP modes as described as follows:

$$E_y(x, z) = \sum_{\rho=0}^{\infty} c_\rho E_{y\rho}(x, z), \quad (6)$$

where c_ρ is the expansion coefficient of the ρ th order AGPP mode supported by the GIWAL, derived from the orthogonality of waveguide modes, which can be calculated using

$$c_\rho = \int_{-\infty}^{\infty} E_y(x, 0) E_{y\rho}^*(x, 0) dx. \quad (7)$$

The interpretation for the beam evolution is mathematically rigorous, as discussed in Sec. 11 in the [Supplementary Material](#). When the coupling grating is extended or local, the electric field at the incident end of the GIWAL can be regarded as $E_y(x, 0) = 1$ V/m or $E_y(x, 0) = \exp\{-2[(x - x_0)/w_0]^2\}$ V/m, where the latter is similar to a Gaussian beam, and $x_0 = 3$ μm and

$w_0 = 1.5$ μm are the incident point on the x axis and characteristic width of the Gaussian beam, respectively. According to Eq. (6), the analytically calculated electric field evolutions are shown in Figs. 2(g) and 2(h), corresponding to the excitation from the extended and local coupling gratings, respectively. The great consistency between analytical results of Figs. 2(g) and 2(h) and numerical simulations of Figs. 2(e) and 2(f) confirms our physical interpretation for the on-chip focusing and the beam evolution of the AGPPs in the GIWAL. Finally, we consider losses in the analytical model with a less rigorous way by adding an absorption coefficient of $\kappa = 0.046$ extracted from the numerical simulation. At this time, the electric field of the beam evolution becomes $E_y(x, z) \exp(-\kappa k_0 z)$, and the corresponding $|E|^2$ are illustrated in Figs. 2(i) and 2(j), respectively. In addition, the self-focusing and self-collimating of Gaussian beams in the GIWAL are also demonstrated (see Sec. 12 in the [Supplementary Material](#) for details).

One of the outstanding characteristics of graphene is that its optoelectronic properties characterized by its surface conductivity σ_g can be actively tuned by adjusting its chemical potential μ_c via electrostatic gates.⁴⁹ This advantage allows us to *in situ* couple the incident light of different frequencies within the ultrabroad spectrum to the AGPP modes while keeping the structure of the coupling grating unchanged. As demonstrated by previous experimental works,^{50,51} electrical control of the chemical potential of graphene can be achieved by depositing metal electrodes on graphene. An additional electron beam lithography process and electronic beam evaporation could be used to define the electrodes. As discussed in Sec. 3 in the [Supplementary Material](#), we set the filling factor and period of the coupling grating to be $f_c = 0.5$ and $\Lambda_c = 561$ nm; thus, the wave vector of the first-order diffraction wave along the z direction is $k_{z,c,1} = 1.12 \times 10^7$ m⁻¹ according to the grating equation $k_{z,c,m} = 2m\pi/\Lambda_c$ ($m = 1, 2, 3, \dots$ is the diffraction order).⁵² To satisfy the phase-matching condition $k_{z,c,1} = \operatorname{Re}(p_c)$, (p_c is the propagation constant along the z direction of the AGPPs supported by the coupling grating) so that the

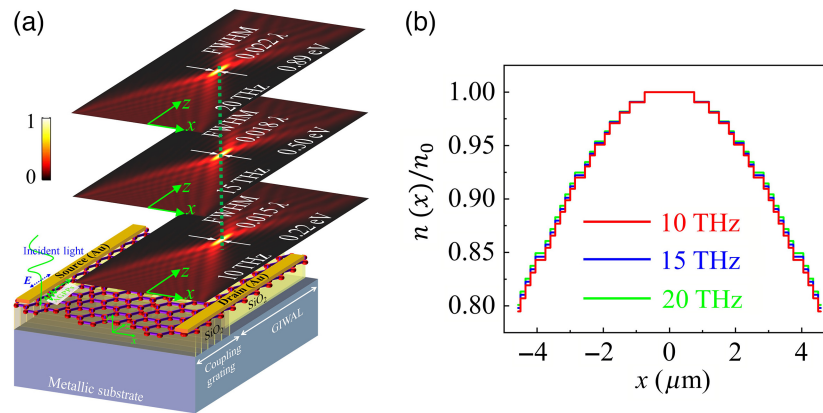


Fig. 3 Achromatic on-chip focusing of the AGPPs in the GIWAL. (a) Normalized electric field $|\mathbf{E}|^2$ of the AGPPs propagating along the z -direction on the $y = 0$ plane in the stepped GIWAL for incident frequencies of 10 THz (lower panel), 15 THz (middle panel), and 20 THz (upper panel), respectively. (b) Refractive index profiles of the stepped GIWAL for incident frequencies of 10 THz (red), 15 THz (blue), and 20 THz (green), respectively. The focal length of the on-chip focusing is $f_L = 10 \mu\text{m}$.

incident light can be efficiently coupled to the AGPPs, we electrically tune the chemical potentials of graphene to be 0.22, 0.50, and 0.89 eV for the incident frequencies of 10, 15, and 20 THz, respectively. The coupling grating couples the incident light to the AGPP modes, which then propagate through the GIWAL along the z direction. The most impressive performance is that the on-chip focusing of the AGPPs is free of chromatic aberration in the GIWAL. As shown in Fig. 3(a), the distributions of the normalized electric field $|\mathbf{E}|^2$ indicate that the focus hardly moves for the incident light of different frequencies in the range from 10 to 20 THz. The physics of this dispersion-free property is attributed to the wavelength-independent refractive index profile of the GIWAL, as shown in Fig. 3(b). This essentially arises from the wavelength-independent and chemical potentially independent variation trend of n_{eff} versus a shown in Fig. 1(c) and Fig. S2(c) in the [Supplementary Material](#). The excellent achromatic on-chip focusing capability demonstrates that the GIWAL is spatially identical for broadband light of different operating wavelengths, enabling on-chip color imaging, signal processing of ultrashort pulses, and broadband optical manipulation. Moreover, the full-width at half-maximum of the focal point is almost always as small as about 0.02λ for the incident lights of different frequencies, which is crucial for broadband high-quality nanoimaging and nanolithography and miniaturized on-chip optoelectronics for long-wavelength applications.

We have demonstrated the achromatic on-chip focusing of the AGPPs in the GIWAL in the previous sections; this may find applications in miniaturized broadband on-chip photonics devices for optical communication and signal processing in the long-wavelength spectrum. As one of the potential prospects based on this remarkable performance, we here indicate the possibility that the proposed GIWAL could act as a spatial inverter for broadband digital optical signals. It is well known that, in computer science and digital signal processing, information is viewed as a string of bits: “0” or “1.”⁵³ To mimic this binary concept, we encode the digital optical signal as “0” or “1,” depending on its intensity of 0 or 1, which can be defined by designing the structure of the coupling grating (see Sec. 3 in the

[Supplementary Material](#) for details). According to the trajectories of rays in Fig. 2(d), if the length of the GIWAL along the z direction is taken as $2f_L$, the spatial positions of the output point and input point of the ray are symmetrical with respect to the line of $x = 0$. Now replace “rays” with “digital optical signals,” which are also symmetrical with respect to the line of $x = 0$. Therefore, at $z = 0$ (the input end of the GIWAL), along the x axis, an incident digital optical signal encoded as “10001000100010001000” is inverted to the sequence “00010001000100010001” at the output end (i.e., $z = 2f_L$) after passing through the GIWAL, as shown in Figs. 4(a) and 4(b). This can also be predicted by our proposed analytical theory (see Sec. 13 in the [Supplementary Material](#) for details). Moreover, different digital optical signals carried by the incident lights of other frequencies, which are generated on demand by designing the structure of the coupling grating, can also be inverted spatially at the output end after passing through the GIWAL, as shown in Figs. 4(c)–4(f). The broadband spatial inverter based on the achromatic GIWAL may play an important role in advanced optical communication technologies, such as wavelength division multiplexing.

3 Materials and Methods

All numerical simulations involved in this study are performed with the commercially available finite-element method package (COMSOL Multiphysics). The adequately thick metallic substrate is made of aluminum with a relative permittivity of $\epsilon_3 = 1 - \omega_p^2/(\omega^2 + i\omega\Gamma)$,⁵⁴ where ω is the angular frequency of the incident light $\Gamma = 0.082 \text{ eV}$ and $\omega_p = 14.754 \text{ eV}$ are the metallic damping constant and plasma frequency, respectively. Moreover, graphene is regarded as an infinitely thin surface, and its optoelectronic properties are described by a surface conductivity σ_g which can be evaluated using a Drude-like expression of $\sigma_g = ie^2\mu_c/[\pi\hbar^2(\omega + i\gamma)]$ at the room temperature and within the frequency band of our interest,^{30,55,56} where $-e$ and \hbar are the charge of an electron and the reduced Planck’s constant, respectively. The relaxation rate and chemical potential are set as $\gamma = 0.1 \text{ meV}$ and $\mu_c = 0.5 \text{ eV}$ unless otherwise stated.

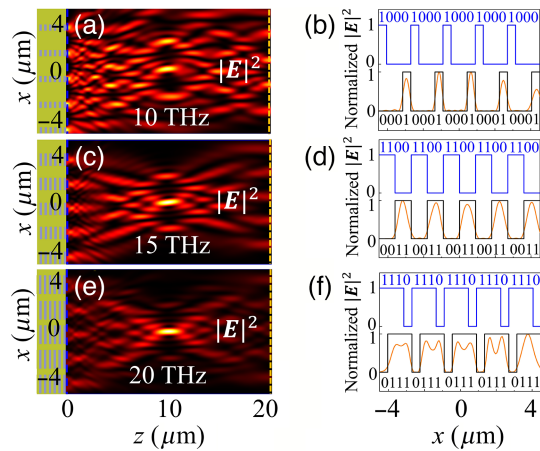


Fig. 4 Spatial inverter for broadband digital optical signals based on the achromatic GIWAL. Normalized electric field $|E|^2$ of the AGPPs propagating along the z direction on the $y = 0$ plane in the GIWAL for incident frequencies of (a) 10 THz, (c) 15 THz, and (e) 20 THz, respectively. The digital optical signals at the input end of the GIWAL are (a) “10001000100010001000,” (c) “11001100110011001100,” and (e) “11101110111011101110,” respectively. Digital encoding of the input signal on the line of $z = 0$ (input end, blue) and the normalized electric field $|E|^2$ of the AGPPs on the line of $z = 2f_L$ (output end, orange) for incident frequencies of (b) 10 THz, (d) 15 THz, and (f) 20 THz, respectively. The black curve is the digital encoding of the output signal. The focal length of the on-chip focusing is $f_L = 10 \mu\text{m}$.

4 Conclusion

We propose a GIWAL to support the propagation of the AGPPs and to enable the achromatic on-chip focusing of the AGPPs with a focus as small as about 0.02λ in the frequency band from 10 to 20 THz, benefiting from the wavelength-independent refractive index profile of the GIWAL. Furthermore, we demonstrate the possibility that the GIWAL could be used as a spatial inverter for broadband digital optical signals, indicating that the GIWAL has great potential value in broadband digital coding communication and digital optical signal processing. Moreover, we provide an analytical understanding to explain the physical process of the achromatic on-chip focusing and beam evolution of the AGPPs in the GIWAL, which agrees very well with numerical simulations. Importantly, the proposed GIWAL can also operate in other wavelength bands of interest or be used as other possible optoelectronic devices by rationally tuning parameters of the structures and materials. In this context, the presented theoretical design principle and analytical physical model are more rapid and computationally compact methods to predict the configuration of such structures.

Code, Data, and Materials Availability

Data underlying the results presented in this paper can be obtained from the authors upon reasonable request.

Acknowledgments

This work was supported in part by the National Natural Science Foundation of China (Grant No. 62105376) and the Guangdong Zhujiang Project (Grant Nos. 2021ZT09X070

and 2021QN02X488). The authors declare no competing financial interests.

References

1. A. H. Atabaki et al., “Integrating photonics with silicon nanoelectronics for the next generation of systems on a chip,” *Nature* **556**(7701), 349–354 (2018).
2. X. Liu et al., “Ultra-broadband and low-loss edge coupler for highly efficient second harmonic generation in thin-film lithium niobate,” *Adv. Photonics Nexus* **1**(1), 016001 (2022).
3. M. Zhang et al., “Supercompact photonic quantum logic gate on a silicon chip,” *Phys. Rev. Lett.* **126**(13), 130501 (2021).
4. L.-T. Feng et al., “Transverse mode-encoded quantum gate on a silicon photonic chip,” *Phys. Rev. Lett.* **128**(6), 060501 (2022).
5. E. Mikheeva et al., “Space and time modulations of light with metasurfaces: recent progress and future prospects,” *ACS Photonics* **9**(5), 1458–1482 (2022).
6. K. Wang et al., “Deep learning spatial phase unwrapping: a comparative review,” *Adv. Photonics Nexus* **1**(1), 014001 (2022).
7. J. Feldmann et al., “Parallel convolutional processing using an integrated photonic tensor core,” *Nature* **589**(7840), 52–58 (2021).
8. Q. He et al., “Monolithic metasurface spatial differentiator enabled by asymmetric photonic spin-orbit interactions,” *Nanophotonics* **10**(1), 741–748 (2021).
9. X. Luo, “Multiscale optical field manipulation via planar digital optics,” *ACS Photonics* (2023).
10. X. Luo, “Metasurface waves in digital optics,” *J. Phys.: Photonics* **2**(4), 041003 (2020).
11. J. M. Luque-González et al., “An ultracompact GRIN-lens-based spot size converter using subwavelength grating metamaterials,” *Laser Photonics Rev.* **13**(11), 1900172 (2019).
12. J. Shen et al., “Ultra-broadband on-chip beam focusing enabled by GRIN metalens on silicon-on-insulator platform,” *Nanophotonics* **11**(16), 3603–3612 (2022).
13. Y. Zhang et al., “Ultra-broadband mode size converter using on-chip metamaterial-based Luneburg lens,” *ACS Photonics* **8**(1), 202–208 (2020).
14. W. Qi, Y. Yu, and X. Zhang, “On-chip arbitrary-mode spot size conversion,” *Nanophotonics* **9**(14), 4365–4372 (2020).
15. S. Hadi Badri and M. M. Gilarlue, “Low-index-contrast waveguide bend based on truncated Eaton lens implemented by graded photonic crystals,” *J. Opt. Soc. Am. B* **36**(5), 1288–1293 (2019).
16. S. Hadi Badri, H. Rasooli Saghari, and H. Soofi, “Polymer multimode waveguide bend based on a multilayered Eaton lens,” *Appl. Opt.* **58**(19), 5219–5224 (2019).
17. S. Li et al., “Universal multimode waveguide crossing based on transformation optics,” *Optica* **5**(12), 1549–1556 (2018).
18. H. Xu and Y. Shi, “Metamaterial-based Maxwell’s fisheye lens for multimode waveguide crossing,” *Laser Photonics Rev.* **12**(10), 1800094 (2018).
19. L. N. Quan et al., “Nanowires for photonics,” *Chem. Rev.* **119**(15), 9153–9169 (2019).
20. A. Karabchevsky et al., “On-chip nanophotonics and future challenges,” *Nanophotonics* **9**(12), 3733–3753 (2020).
21. F. J. Garcia-Vidal et al., “Spoof surface plasmon photonics,” *Rev. Mod. Phys.* **94**(2), 025004 (2022).
22. E. Prinz et al., “Functional meta lenses for compound plasmonic vortex field generation and control,” *Nano Lett.* **21**(9), 3941–3946 (2021).
23. J. Ye, Y. Li, and S. Qu, “On-chip orbital angular momentum sorting with a surface plasmon polariton lens,” *J. Lightwave Technol.* **39**(5), 1423–1428 (2021).
24. L. Verslegers et al., “Deep-subwavelength focusing and steering of light in an aperiodic metallic waveguide array,” *Phys. Rev. Lett.* **103**(3), 033902 (2009).
25. Y. Jiao et al., “Self-focusing and self-bending of surface plasmons in longitudinally modulated metasurfaces,” *Opt. Commun.* **450**, 136–140 (2019).

26. Y. Wang et al., "Spatiotemporal manipulation on focusing and propagation of surface plasmon polariton pulses," *Opt. Express* **28**(22), 33516–33527 (2020).
27. Y. Wang et al., "Drawing structured plasmonic field with on-chip metalens," *Nanophotonics* **11**(9), 1969–1976 (2022).
28. W. Liu et al., "Polychromatic nanofocusing of surface plasmon polaritons," *Phys. Rev. B* **83**(7), 073404 (2011).
29. Z. Fei et al., "Gate-tuning of graphene plasmons revealed by infrared nano-imaging," *Nature* **487**(7405), 82–85 (2012).
30. P. A. D. Gonalves and N. M. R. Peres, *An Introduction to Graphene Plasmonics*, World Scientific (2016).
31. Q. Guo et al., "Infrared nanophotonics based on graphene plasmonics," *ACS Photonics* **4**(12), 2989–2999 (2017).
32. T. Nagatsuma, G. Ducournau, and C. C. Renaud, "Advances in terahertz communications accelerated by photonics," *Nat. Photonics* **10**(6), 371–379 (2016).
33. Y. Yang et al., "Terahertz topological photonics for on-chip communication," *Nat. Photonics* **14**(7), 446–451 (2020).
34. J. Nong et al., "Enhanced graphene plasmonic mode energy for highly sensitive molecular fingerprint retrieval," *Laser Photonics Rev.* **15**(1), 2000300 (2021).
35. M. B. Lundeborg et al., "Thermoelectric detection and imaging of propagating graphene plasmons," *Nat. Mater.* **16**(2), 204–207 (2017).
36. A. Woessner et al., "Electrical 2π phase control of infrared light in a 350-nm footprint using graphene plasmons," *Nat. Photonics* **11**(7), 421–424 (2017).
37. L. Lu et al., "Dynamically controlled nanofocusing metalens based on graphene-loaded aperiodic silica grating arrays," *Opt. Express* **30**(4), 5304–5313 (2022).
38. P. Alonso-González et al., "Acoustic terahertz graphene plasmons revealed by photocurrent nanoscopy," *Nat. Nanotechnol.* **12**(1), 31–35 (2017).
39. P. A. D. Gonçalves et al., "Strong light–matter interactions enabled by polaritons in atomically thin materials," *Adv. Opt. Mater.* **8**(5), 1901473 (2020).
40. T. G. Rappoport et al., "Topological graphene plasmons in a plasmonic realization of the Su–Schrieffer–Heeger model," *ACS Photonics* **8**(6), 1817–1823 (2021).
41. I.-H. Lee et al., "Graphene acoustic plasmon resonator for ultrasensitive infrared spectroscopy," *Nat. Nanotechnol.* **14**(4), 313–319 (2019).
42. I. Epstein et al., "Far-field excitation of single graphene plasmon cavities with ultracompressed mode volumes," *Science* **368**(6496), 1219–1223 (2020).
43. X. Wang et al., "Self-focusing and the Talbot effect in conformal transformation optics," *Phys. Rev. Lett.* **119**(3), 033902 (2017).
44. J. Chen et al., "Conformally mapped Mikaelian lens for broadband achromatic high resolution focusing," *Laser Photonics Rev.* **15**(5), 2000564 (2021).
45. G. B. Hocker and W. K. Burns, "Mode dispersion in diffused channel waveguides by the effective index method," *Appl. Opt.* **16**(1), 113–118 (1977).
46. H. G. Unger, *Planar Optical Waveguides and Fibres*, Oxford University Press (1977).
47. A. Yariv and P. Yeh, *Photonics: Optical Electronics in Modern Communications*, Oxford University Press (2007).
48. Z. Zhang et al., "Nonparaxial mode-size converter using an ultracompact metamaterial Mikaelian lens," *J. Lightwave Technol.* **39**(7), 2077–2083 (2021).
49. C. Zeng et al., "Graphene-empowered dynamic metasurfaces and metadevices," *Opto-Electron. Adv.* **5**(4), 200098 (2022).
50. H. Hu et al., "Far-field nanoscale infrared spectroscopy of vibrational fingerprints of molecules with graphene plasmons," *Nat. Commun.* **7**(1), 12334 (2016).
51. W. Gao et al., "Excitation and active control of propagating surface plasmon polaritons in graphene," *Nano Lett.* **13**(8), 3698–3702 (2013).
52. F. Lu et al., "Mode evolution and nanofocusing of grating-coupled surface plasmon polaritons on metallic tip," *Opto-Electron. Adv.* **1**(6), 180010 (2018).
53. B. C. Kress and P. Meyrueis, *Applied Digital Optics*, John Wiley & Sons (2009).
54. M. A. Ordal et al., "Optical properties of fourteen metals in the infrared and far infrared: Al, Co, Cu, Au, Fe, Pb, Mo, Ni, Pd, Pt, Ag, Ti, V, and W," *Appl. Opt.* **24**(24), 4493–4499 (1985).
55. T. G. Rappoport et al., "Understanding the electromagnetic response of graphene/metallic nanostructures hybrids of different dimensionality," *ACS Photonics* **7**(8), 2302–2308 (2020).
56. S. H. Park et al., "Accessing the exceptional points in a graphene plasmon–vibrational mode coupled system," *ACS Photonics* **8**(11), 3241–3248 (2021).

Zhiyong Wu received his master's degree in optics from Shenzhen University in 2021. He is currently a PhD student at the School of Microelectronics Science and Technology of Sun Yat-sen University, China. His research focuses on the physical properties of graphene plasmonics and on-chip optoelectronics based on graphene plasmons.

Zhengji Xu received his BEng and PhD degrees from Nanyang Technological University, Singapore, in 2010 and 2016, respectively. He is an associate professor and assistant dean at the School of Microelectronics Science and Technology, Sun Yat-sen University, China. He worked as a scientist at the Institute of Microelectronics, A*STAR (Agency for Science, Technology and Research), Singapore, from November 2017 to March 2020. His research interests include flat optics, plasmonics, nanofabrication, and nanophotonics integration.